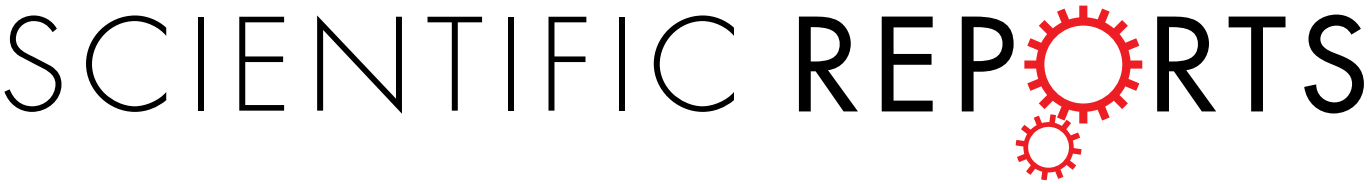

OPEN

Structural, electrical and magnetic properties of Nd – A – CoO_3 (A = Sr, Ca) Perovskite Powders by Mechanical Alloying

Received: 14 June 2017
Accepted: 13 August 2018
Published online: 30 August 2018

Celal Kursun[1,2], Musa Gogebakan[1], Esra Uludag[1], Mehmet S. Bozgeyik[1] & Fatih Samil Uludag[3]

In this work, $NdCoO_3$ (NCO), $Nd_{0.8}Sr_{0.2}CoO_3$ (NSCO) and $Nd_{0.9}Ca_{0.1}CoO_3$ (NCCO) perovskite cobaltites were synthesised by mechanical alloying method. Structural evolutions, magnetic and electrical properties of these perovskite were systematically examined through X-ray diffraction (XRD), scanning electron microscopy with energy-dispersive X-ray detection (SEM-EDX), transmission electron microscopy (TEM), differential scanning calorimetry (DSC), vibration sample magnetometer (VSM) and impedance analyser (IA). The XRD and SEM results revealed that the microstructure of the perovskite materials changed during mechanical alloying. The average crystallite size of the perovskite materials was calculated by Debye Scherrer equation and was confirmed by TEM, and it was determined ~19 nm. From the VSM results, the all perovskites had soft ferromagnetic properties. IA measurements showed that relatively dielectric constants of the perovskites decreased with increasing frequency. Therefore, for the first time, nanostructured NCO, NSCO and NCCO perovskites exhibiting good properties were produced in only two steps which are milling and heating.

Rare earth perovskite cobaltite with the general composition of *Re*CoO3 and the doped mixed oxides with the general composition of $Re_{1-x}A_xCoO_3$ have been extensively studied for their potential applications, where *Re* is for trivalent rare earth elements such as La, Pr, Nd, Eu, Gd, Ny and *A* is for divalent alkaline earth elements such as Ba, Sr, Ca, P or Mg. The potential applications of perovskite materials include cathodes in solid oxide fuel cells (SOFC), sensor materials for thermoelectric conversion, oxygen separation membranes, catalysts, non-volatile memories, magnetic memory media, refractory materials, automotive exhaust oxidation catalysts, oxygen electrode catalysts in aqueous alkaline solution batteries and solar cells[1–11].

The ideal perovskite structure is shown in Fig. 1a. The primitive cell of the ideal cubic perovskite structure can be seen in Fig. 1b. In ideal perovskite-type structure, A cation is 12-fold coordinated and B (Co) cation is 6-fold coordinated with oxygen anions. The perovskite oxides exhibit super conductivity, colossal magneto resistance (CMR), ferroelectric, photo catalytic and unique thermoelectric (TE) properties[12–15]. In addition, for some cobaltites like $NdCoO_3$, the high Seebeck coefficient was reported near the room temperature[16–18]. The ferromagnetic cobaltites have been drawing attention for their large magnetic moment and colossal magneto resistance effect (CMR). The cobalt oxides have properties of hopping of e_g electron double-exchange interactions (DE) between Co^{+3} and Co^{+4} ions which depend on the Co-O-Co bond angle and Co-O bond length like in manganates[18,19].

Both trivalent and tetravalent cobaltites exhibit two magnetic transitions with increasing temperature. One of them is the spin-state transition, also known as the metal-insulator transition, which is a paramagnetic-ferromagnetic (PM-FM) phase transition (Jahn-Teller distortion) at the critical Curie temperature (T_C). The second transition is about the low spin state, intermediate spin state and high spin state that exist in Co ions. However, the low spin state (LS) is $t_{2g}^6\ e_g^0$ with S = 0 for Co^{+3} ion and $t_{2g}^5\ e_g^0$ with S = 1 for Co^{+4} ion, the intermediate spin state (IS) is $t_{2g}^5\ e_g^1$ with S = 1 for Co^{+3} ion and $t_{2g}^4\ e_g^1$ with S = 3/2 for Co^{+4} ion and the

[1]Department of Physics, Faculty of Art and Sciences, Kahramanmaras Sutcu Imam University, Kahramanmaras, 46100, Turkey. [2]Department of Electronics and Automation, Vocational School of Technical Sciences, Kahramanmaras Sutcu Imam University, Kahramanmaras, 46100, Turkey. [3]Department of Health Physics, Institute of Medical Sciences, Yildirim Beyazit University, Ankara, Turkey. Correspondence and requests for materials should be addressed to C.K. (email: celalkursun@hotmail.com)

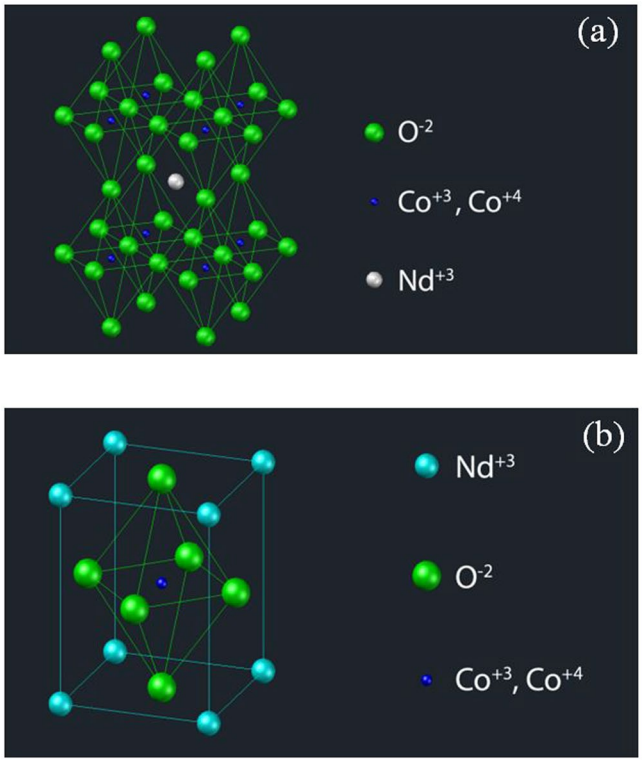

Figure 1. (**a**) Ideal cubic perovskite structure. (**b**) Ideal cubic structure in primitive cell.

finally, high spin state (HS) is $t_{2g}^4 e_g^2$ with S = 2 for Co^{+3} ion and $t_{2g}^3 e_g^2$ with S = 5/2 for Co^{+4} ion[20–25]. These are nearly degenerate in energy. When the crystal structure changes, the spin transitions can be observed. Because of this reason both the spin state and the ionic radius of Co^{+3} ion increase (Ionic radius for Co^{+3} $r_{LS} = 0.545$ Å, $r_{IS} = 0.560$ Å and $r_{HS} = 0.610$ Å). This change can be explained by the Hund energy in the CoO_6 octahedron, Jahn Teller effect, double-exchange mechanism and collerated polarons[26–28].

When the ferromagnetic transition temperature (T_C) decreases, B-O-B (Co-O-Co) bond angle and hence Goldschmidt factor introduced a tolerance factor, "t" also decreases. However, the distortions in the lattice are determined owing to the value of tolerance factor. The tolerance factor is calculated by Eq. 1,

$$t = \frac{r_A - r_0}{\sqrt{2}(r_B - r_0)} \tag{1}$$

in consequence of the relation between the ionic radii holds:

$$r_A + r_0 = \sqrt{2}(r_B + r_0) \tag{2}$$

where r_A is the ionic radius of A site cation (A = Nd, Sr, Ca), r_0 is the ionic radius of oxygen and r_B is the ionic radius of B site cation (B = Co).

The value of tolerance factor "t" is stable between 0.75 and 1.0. If the value of tolerance factor is 1, the bond angle is 180°. When the angle is 180° or approaches to this value, the best overlap is achieved[29–32]. The effect of the value of the tolerance factor on bond angles were schematized in Fig. 2. It can be obviously seen in Fig. 2 that the bond angle is not 180° (Fig. 2a) if the value of tolerance factor doesn't close to 1, however, if it is 1 (Fig. 2b), the best overlap exists.

The perovskite oxides can be synthesised by following methods: solid state reactions, a citric acid assisted soft chemistry synthesis, the wet chemistry-polymerizable complex method, the glycine- nitrate process method, citrate- nitrate combustion method, reactive grinding, the polymeric precursor method, sol-gel method, electro-spinning method, polymerized gel combustion, co-precipitation, glycothermal etc.[33–44]. However, in the present study, mechanical alloying (MA) method was used to produce these materials as a new technique.

MA has been used to synthesis quality powders of compounds and alloys with well-controlled microstructures and morphologies[45]. In this technique, materials are produced on powder forms, which can be easily compacted in desired shapes and dimensions for practical application. Working principle of MA is schematized in Fig. 3. As shown in Fig. 3, the powders in the stainless steel cups remain between balls. The balls collide with each other while the cups and planetary disk are turning opposite direction. Afterwards the powders are diffused into each other with the effect of colliding balls. The structural changes of the powders which subject to the ball collisions during the milling operation are schematized in Fig. 4. The powders have different size distribution and shapes at initially (Fig. 4a), however, their particle size and shapes change with increasing milling time and they diffuse into each other because of the cold welding and fracturing of the particles as it seen Fig. 4b and c. With further milling

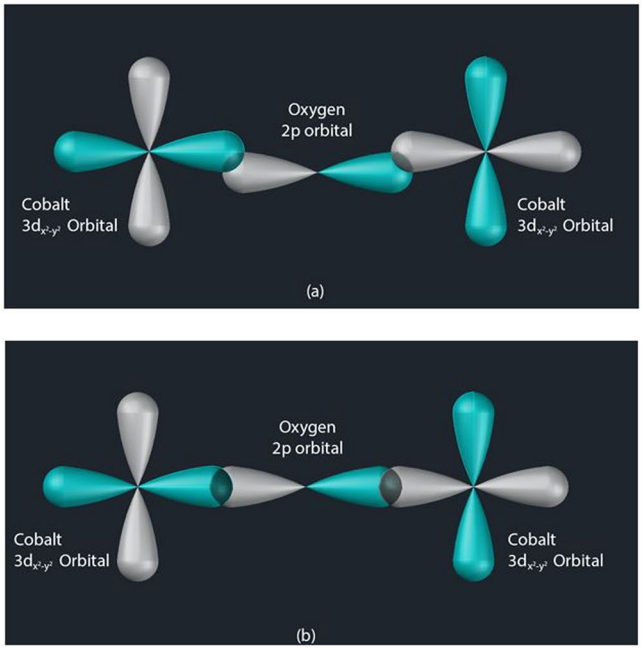

Figure 2. The overlap influence of Co-O-Co angle. (**a**) When the Co-O-Co angle can not achieved 180°, overlap is small. (**b**) While the Co-O-Co angle is 180°, overlap is well.

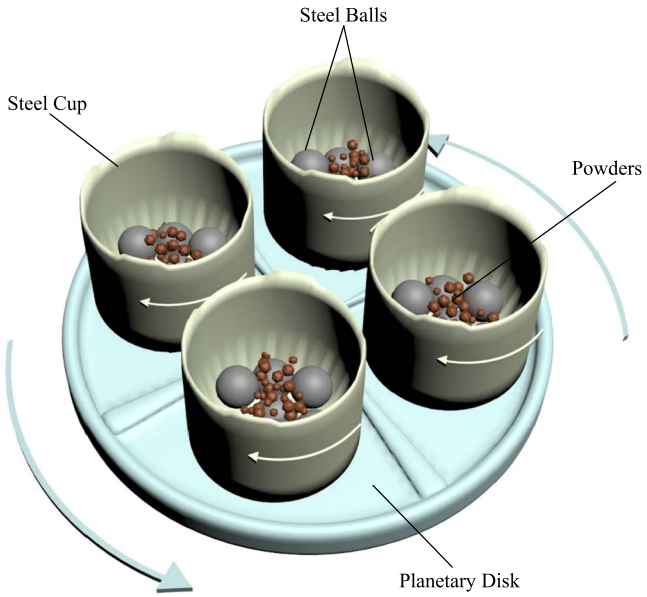

Figure 3. Schematic diagram of mechanical alloying.

time it can be seen that the particle becomes smaller and it appears to approach a spherical shape in Fig. 4d. In this final stage, the homogeneity of the powders is the highest.

For the first time the perovskite cobaltites such as Nd – A – CoO_3 (A = Sr, Ca) are produced in the form of powder by this method without any pre-annealing or sintering, acidic solution and alcohol for solvation. This technique allows to obtain the perovskites in only two steps: milling and heating. In addition to the easy production of the perovskite cobaltite oxides by mechanical alloying, the microstructure analysis can also be done easily[45,46].

Methods

The perovskite cobaltates, $NdCoO_3$, $Nd_{0.8}Sr_{0.2}CoO_3$ and $Nd_{0.9}Ca_{0.1}CoO_3$ were prepared by mixing $Nd(NO_3)_3.6H_2O$ (Aldrich, 99.9%), $Sr(NO_3)_2$ (Acros Organics, 99.8%), $Ca(NO_3)_2.4H_2O$ (Acros Organics, 99.9%) and $Co(NO_3)_2.6H_2O$ (Merck, 99.7%) which are measured stoichiometric amount of nitrate salts. The mixture of the powders with the stainless steel balls was charged into a stainless steel cup (125 ml). The powders were

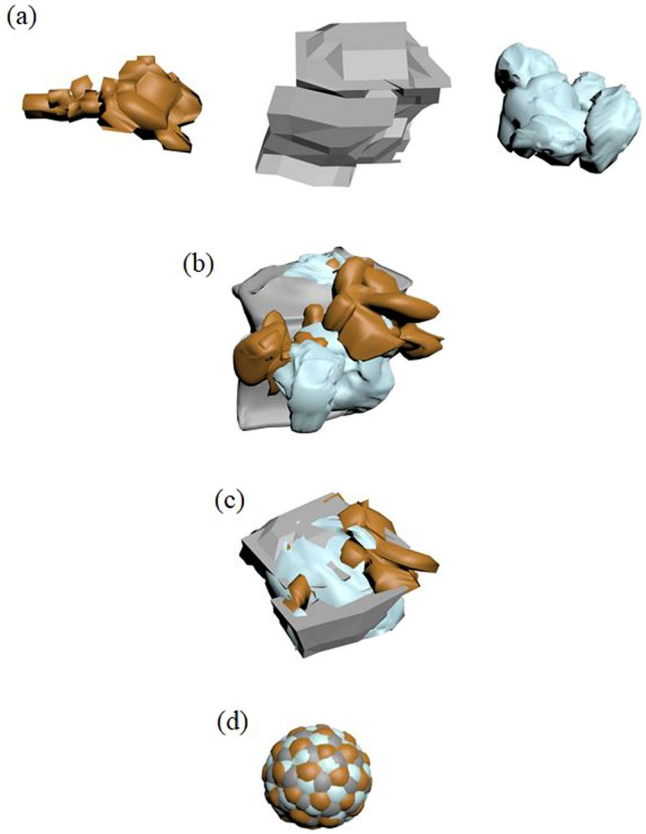

Figure 4. Schematic diagram of the microstructure evolution for powders during MA process.

mechanically milled in planetary ball mills (Fritsch Pulverisette 5) at room temperature. A ball to mass powder ratio is 5:1. This method was performed at the rotation speed of 300 rpm and the whole mechanical milling process continued for 4 h, 8 h, 12 h, 24 h and 48 h for each compounds. Moreover, after each 20 min of ball milling, mechanical milling was interrupted for 20 min in order to cool down the vials. After production processes by ball milling, mechanically milled for 48 h NCO, NSCO and NCCO powders were heated with the heating rate of 20 °C min^{-1} up to 1000 °C, which the powders were annealed for 2 h in a furnace with argon atmosphere.

Crystalline phases of the whole samples during milling were identified by X-Ray diffraction (XRD) using a Philips X'Pert PRO diffractometer with Cu Kα radiation ($\lambda = 0.154$ nm). The thermal behaviour was examined by Perkin-Elmer Sapphire differential scanning calorimetry (DSC) under inert gas atmosphere using continuous heating mode with the heating rate of 40 K min^{-1} for all perovskite powders. The microstructural analysis was studied by SEM with a JEOL JCM 5000 scanning electron microscope at an acceleration voltage of 10 kV. Transmission electron microscopy (TEM) investigation of the $NdCoO_3$ was performed by a Phillips CM-20 operating at 200 kV. For dielectric study samples were mixed with polyvinyl alcohol (PVA) as a binder and pressed into cylindrical pellets of 13 mm diameter, under an isostatic pressure of 5×10^6 Nm^{-2} using a hydraulic press. Then the pellets were sintered at an optimized temperature of 400 °C for 30 min. in air. Dielectric properties were measured at room temperature in a wide frequency range of 100 Hz to 1 MHz using an impedance analyser HP4294A. Magnetic characteristics were studied up to a field of 1.5 T by Vibrating Sample Magnetometer (VSM) Lake Shore 7400.

Results and Discussion

Microstructural evaluation. The microstructural evolutions of the NCO, NSCO and NCCO powders were performed by SEM to reveal the morphological changes and the decrease in the particle size during mechanical milling. Figure 5 presents the SEM micrographs of un-doped $NdCoO_3$ powders. As shown in Fig. 5a, the unmilled $Nd(NO_3)_3.6H_2O$ and $Co(NO_3)_2.6H_2O$ salt particles had irregular morphology. However, $Nd(NO_3)_3.6H_2O$ powder particles were nearly uniform in size with hexagonal morphology. Besides, the sizes of $Co(NO_3)_2.6H_2O$ powders were smaller than the sizes of $Nd(NO_3)_3.6H_2O$ powders. After 8 h of milling (Fig. 5b), the particles begin to agglomerate because of the cold welding by colliding balls. Thus, the microstructure of powders was changed. The colliding force between balls and $Nd(NO_3)_3.6H_2O$ and $Co(NO_3)_2.6H_2O$ powders were largely used in the plastic deformation process. For the powders subjected to 24 h of mechanical milling, it can be seen clearly in Fig. 5c that the average particle size of the powder decreased due to fracturing. At this stage, the powder attached strongly each other and they had absolutely different shapes from initial form. For the higher milling time up to 48 h, the size distribution and shapes of the powders have continued to change. As it seen Fig. 5d after 48 h of milling it resulted in the formation of submicrometer particles with an average particle size of ~10 μm. One can obviously

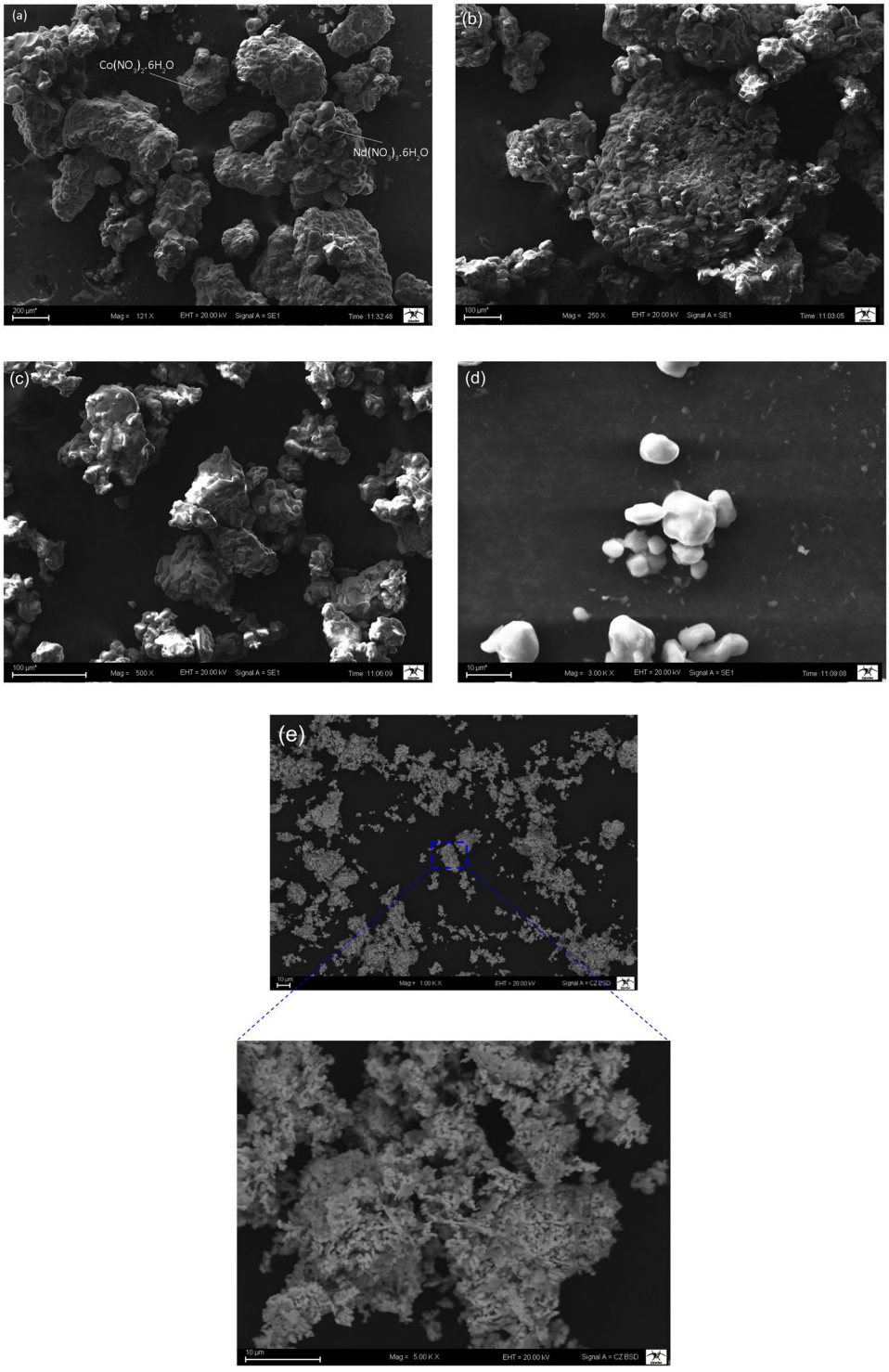

Figure 5. Morphological changes of the $NdCoO_3$ (NCO) powders as a function of the milling time (**a**) 0 h; (**b**) 8 h; (**c**) 24 h; (**d**) 48 h; (**e**) after heat treatment at 1000 °C for 2 h for 48 h milling.

see that the powder particles had more homogeneity and appeared to a spherical shape in Fig. 5d. Figure 5e shows SEM images of perovskite NCO powders after heat treatment at 1000 °C for 2 h after 48 h milling. According to Fig. 5e, the spherical shape of the powders (in Fig. 5d) was changed and transformed to shapeless form with porous like a sponge rubber.

In the rare-earth perovskite with general formula ABO_3, the structural distortions are usually occurred. While Sr or Ca replace Nd in the crystal lattices of $Nd_{0.8}Sr_{0.2}CoO_3$ and $Nd_{0.9}Ca_{0.1}CoO_3$, respectively, the average ionic radius in A site changes. Similarly, these ionic mismatches were observed for the doped perovskite cobaltites. The ionic radii mismatch in A-site lead to size variance σ^2 which is

Elements	Nd^{+3}	Sr^{+2}	Ca^{+2}	Co^{+3}	Co^{+4}	O^{-2}
Coordinate	IX	IX	IX	VI	VI	VI
Ionic Radius Angstrom (Å)	1,163	1,31	1,18	0,545	0,53	1,4

Table 1. Ionic radius and coordinates of A site and B site elements.

Content (Sr, Ca)	$\langle r_A \rangle$ (Å)	$\langle r_B \rangle$ (Å)	r_O (Å)	t (tolerance factor)	Ionic mismatch (σ^2) Å^2
0.0	1,163	0,5450	1,4	0,9318	0
0.2 Sr	1,1924	0,5420	1,4	0,9439	0,00345
0.1 Ca	1,1647	0,5435	1,4	0,9331	0,00002

Table 2. Tolerance factors and ionic mismatches of perovskite materials.

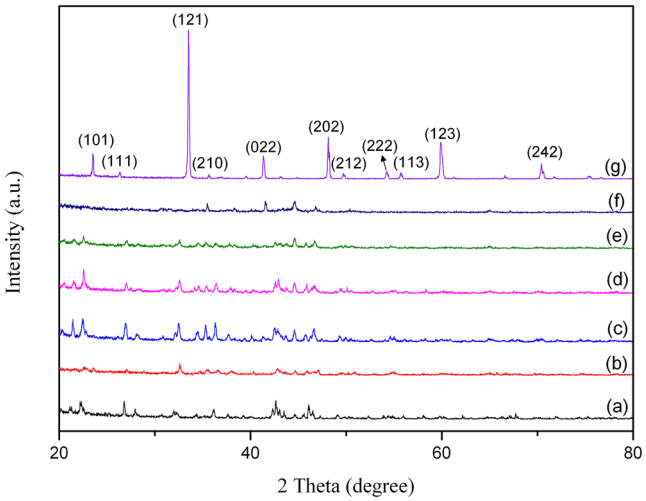

Figure 6. X-ray diffraction patterns of $NdCoO_3$ (NCO) powders as a function of mechanical alloying time: (**a**) 0 h; (**b**) 4 h; (**c**) 8 h; (**d**) 12 h; (**e**) 24 h; (**f**) 48 h and (**g**) subsequent 2 h heat treatment at 1000 °C for 48 h milling.

$$\sigma^2 = (\sum_i x_i r_i^2) - \langle r_i \rangle^2 \tag{3}$$

The ionic radius of the A site and B site elements and their coordinates are listed in Table 1.

Table 2 shows the tolerance factors and ionic mismatches for each of the perovskite samples. It is well known that the tolerance factor changes between 0.75 and 1.00[47]. According to the Table 2 the tolerance factors of Nd – A – CoO_3 (A = Sr, Ca) are in the range of 0.93–0.94. These results are consonant with literature.

The structural features of NCO, NSCO and NCCO perovskite powders were characterised by X-ray diffraction. Figures 6–8 show the XRD patterns of the NCO, NSCO and NCCO perovskites. As shown in Figs 6–8, all the mechanically milled the powders indicate certain behaviours during mechanical milling. Because of the heavy deformation, repeated fracturing and cold welding of the powders, the diffraction lines shift and the peak broadenings increase as well as the diffraction lines of solute disappear with increasing milling time. As a result of the increase in internal strain and reduction in grain size, the peaks broadening of the XRD peaks has taken place during mechanical alloying. The XRD patterns of 2 h heat treatment at 1000 °C after 48 h milling for perovskite NCO, NSCO and NCCO powders are also shown in Figs 6g, 7g and 8g, respectively. These perovskite peaks are in agreement with the earlier reported studies for $NdCoO_3$ perovskite materials by salt-assisted combustion process[44] and sol-gel technique[46].

According to the results of 0 h–24 h milling of the powders, the sharp crystalline peaks which belong to nitrate salts broadened and their intensities decreased in Figs 6(a–e), 7(a–e) and 8(a–e). It can be seen clearly in Figs 6–8(f) that most of the elemental peaks disappeared after 48 h of milling. These peaks which disappear after 48 h milling time is usually attributed to the creation of nanostructured solid solution[48]. The all powders subjected to heat treatment at 1000 °C for 2 h after 48 h milling. From the XRD patterns of NCO, NSCO and NCCO powders after this process, it can be obviously seen in Figs 6–8(g) that the crystallite peaks with very sharp and high intensity were obtained. These peaks are characteristic peaks of the perovskite materials which are identified by ICSD code 082078[49]. The XRD analyses reveals the formation of orthorhombic $NdCoO_3$ (space group: Pnma) in all samples (Figs 6–8(g)).

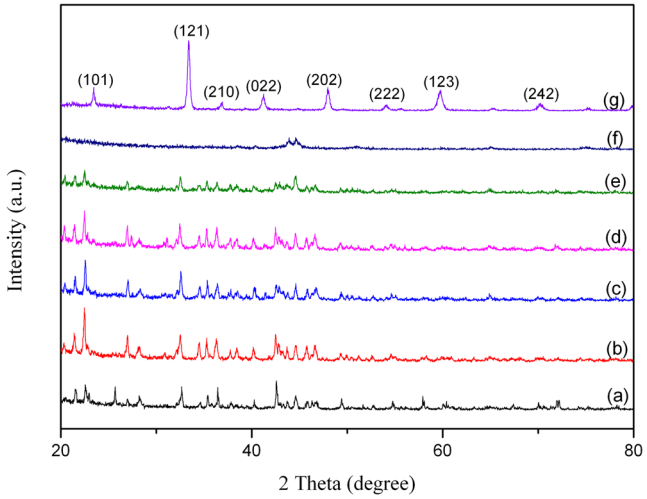

Figure 7. X-ray diffraction patterns of $Nd_{0.8}Sr_{0.2}CoO_3$ (NSCO) powders as a function of Mechanical alloying time: (**a**) 0 h; (**b**) 4 h; (**c**) 8 h; (**d**) 12 h; (**e**) 24 h; (**f**) 48 h and (**g**) subsequent 2 h heat treatment at 1000 °C for 48 h milling.

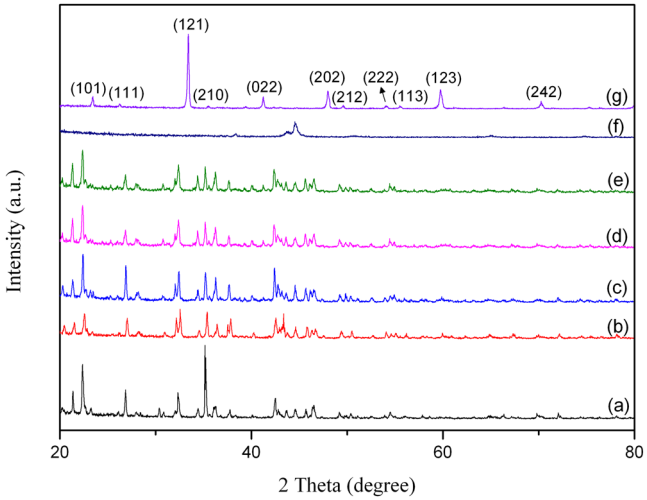

Figure 8. X-ray diffraction patterns of $Nd_{0.9}Ca_{0.1}CoO_3$ (NCCO) powders as a function of Mechanical alloying time: (**a**) 0 h; (**b**) 4 h; (**c**) 8 h; (**d**) 12 h; (**e**) 24 h; (**f**) 48 h and (**g**) subsequent 2 h heat treatment at 1000 °C for 48 h milling.

Figure 9a–c shows the EDX analysis of the perovskite NCO, NSCO and NCCO powders. According to Fig. 9a–c, the elemental peaks which belong to Nd, Co and O can be seen clearly for all perovskite powders. However, Sr and Ca elemental peaks are also observed for NSCO and NCCO perovskites, respectively. It is because these elemental peaks exist in their composition in contrary NCO perovskite which are occured Nd, Co and O. The observed Sr and Ca elements from EDX analysis couldn't be identified in XRD pattern (Figs 6–8) because of their very few amount in the NSCO and NCCO. It may be also attributed that Sr and Ca solve into the Nd or Co elements. The similar solving process was observed in previously work at mechanical alloying systems in literature[45,48].

Crystallite size evaluation. The crystalline sizes of NCO, NSCO and NCCO powders are calculated from broadening of XRD peaks by Scherrer equation[45]

$$D = \frac{0.9\lambda}{B\cos\theta} \tag{4}$$

where D is the average crystallite size, λ the wave length of using X-ray, B the full width (in radians) at half maximum intensity and θ the diffraction Bragg angle.

The crystallite size evolutions of NCO, NSCO and NCCO powders as function of milling time are presented in Fig. 7. As seen from Fig. 10, the crystallite sizes of the powders decreased sharply and were calculated ~20 nm after 12 h ball milling. The average crystallite sizes of NCO, NSCO and NCCO powders reach the lowest values,

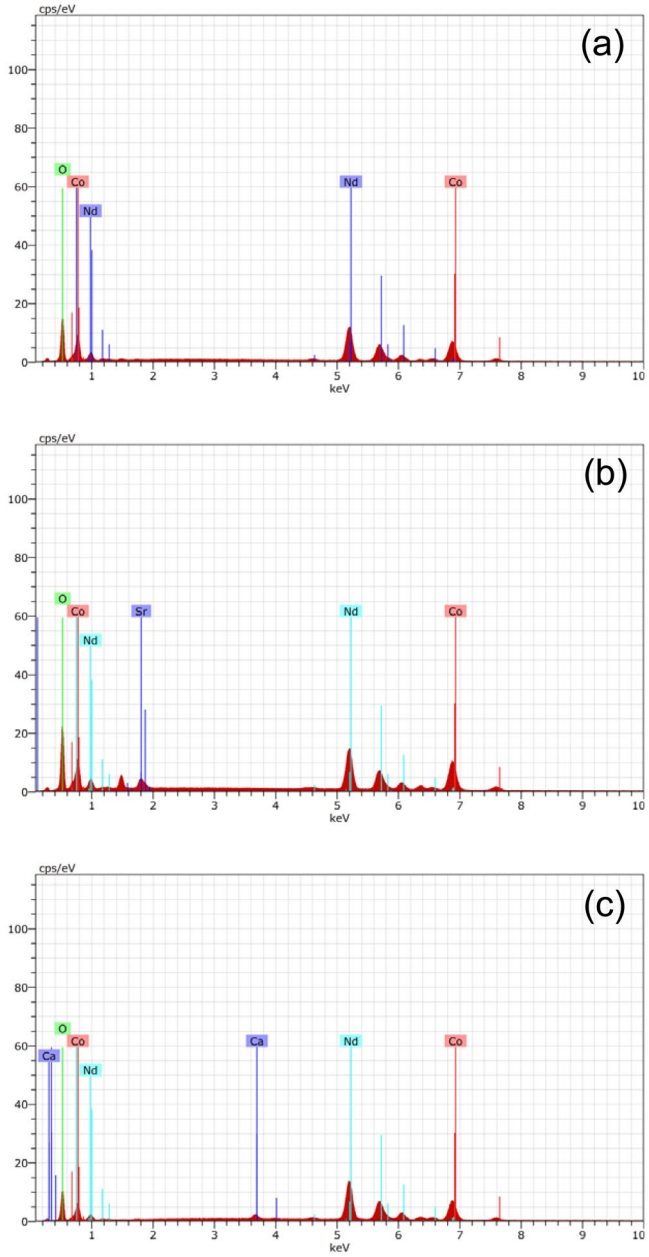

Figure 9. EDX analysis of the perovskite NCO, NSCO and NCCO powders.

18.2 nm, 19.2 nm and 19.7 nm, respectively, after 48 h of milling time. The crystallite size evolution of NCO powder was also monitored by TEM to predicate the crystallite size of obtained by XRD. Figure 11 shows typical dark field TEM image of the NCO for 48 h milling. As it seen clearly Fig. 11 the crystallite size of the NCO is below 20 nm. This result is consonant with the crystallite size value of NCO calculating by XRD data.

Magnetic and electrical properties. Figure 12 indicates steeply increasing magnetization in very narrow hysteresis loops. According to the related hysteresis loops in Fig. 12 and Table 3 low coercivity (HC) ranging from 170 to 244 G and small remnant magnetization (Mr) between 2.085 and 2.254 emu/g revealed that the magnetic behaviour looks like soft ferromagnetic.

These values are far away from those related values of superparamagnetics which have theoretically no hysteresis loop by means of zero remanence and zero coercivity, i.e., just a sigmoidal S like shape. As a matter of fact, anisotropy, interaction of identical particle, and crystallite size distributions have the potential to alter the M-H hysteresis curves. Hence, experimentally negligible small (almost zero) remanence magnetization and coercive field (a few Oersted) have been measured for ferro/ferrimagnetic nanoparticles which have the size distribution ranging from a few nanometers to few tenth of nanometers. Such a nanoparticle system behaves superparamagnetic hysteresis curve. Moreover, soft ferromagnetic materials composed of nanoparticles below certain size could show superparamagnetic behaviour.

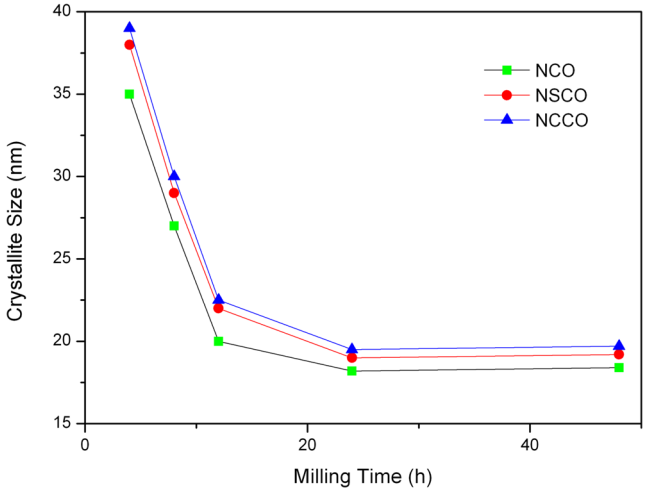

Figure 10. Crystal size of mechanically milled NCO, NSCO and NCCO powders as a function of milling time.

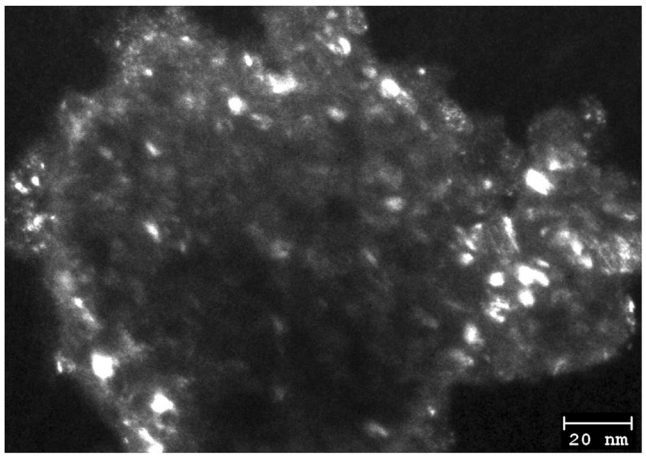

Figure 11. Typical dark field TEM image of the perovskite NCO for 48 h milling.

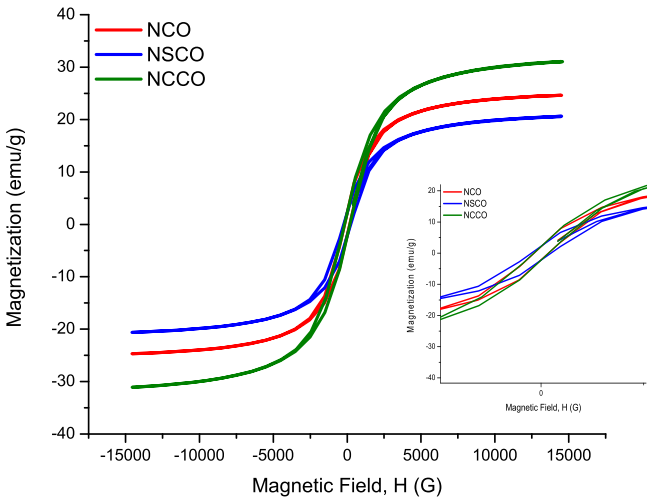

Figure 12. Room temperature magnetization vs. magnetic field (M-H) measurements of NCO, NSCO, and NCCO.

Sample	H_{C-} (G)	H_{C+} (G)	M_{r-} (emu/g)	M_{r+} (emu/g)	M_{S-} (emu/g)	M_{S+} (emu/g)	M_r/M_{S-}	M_{r+}/M_{S+}
NCO	−170	178	−2.143	2.085	−24.631	24.586	0.087	0.085
NSCO	−233	244	−2.249	2.196	−20.551	20.649	0.109	0.106
NCCO	−177	184	−2.254	2.148	−31.017	31.124	0.073	0.069

Table 3. Tabulated hysteresis loop parameters.

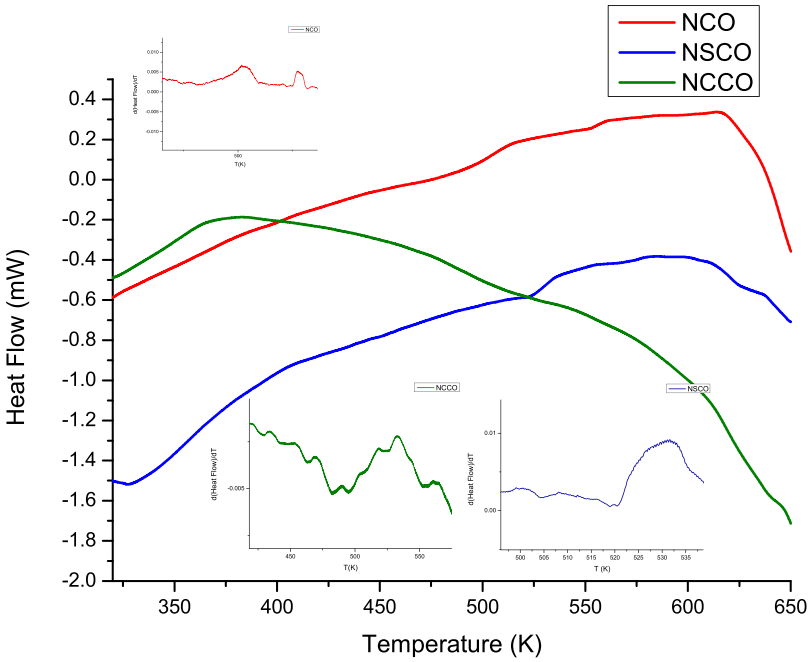

Figure 13. Thermal analysis of the samples by means of DSC. Inset figures shows the first derivative of heat flow with respect to temperature which indicates the related Curie Temperatures (T_C).

On the contrary, according to Fig. 12 and Table 3 all samples present appreciable hysteresis curves with slim width and fairly small amount of remanence magnetizations and coercive fields. As shown in the inset of Fig. 12 magnetization gradually increases with field. In addition to this, the M_r/M_s ratio of a hysteresis curve is ranging from 0.085 to 0.109 which are quite small, thereby, the curves look like S form not square like. Hence, such a hysteresis loop could hardly be considered as superparamagnetic behaviour.

Although Zero Field Cooling (ZFC) and Field Cooling (FC) Magnetization versus Temperature (M-T), of course, give additional information on magnetic behavior, above discussion on the basis of the room temperature M-H measurements and summarized parameters in Table 3 are enough to judge the magnetic behavior of the samples. As a matter of fact, ZFC and FC Magnetization versus Temperature (M-T), of course, give additional information on magnetic behavior for instance related Curie temperature (T_C), thermal analysis like Differential Scanning Calorimetry (DSC) is able to determine T_C of a magnetic material. So, the DSC measurements carried out for all the samples indicated that Curie temperatures (T_C) were all highly above room temperature as seen in Fig. 13. Therefore, T_C of NCO, NSCO, and NCCO were precisely determined from DSC measurements according to the endothermic peaks and inset figures which show the first derivative of the heat flow with respect to temperature by the following values of 462, 520, and 495 K, respectively.

Temperature dependent magnetization (M-T) were performed by means of Zero Field Cooling (ZFC) and Field Cooling (FC) measurements between the limited temperature ranges of 2–380 K at 100 Oe. Corresponding M-T curves are presented in Fig. 14. Common behavior of the ZFC and FC curves is that the ZFC magnetization decreases continuously by decreasing temperature while that of FC increase. The ZFC curve of NCO presents a peak at around 350 K which is interpreted as the Blocking temperature (T_B). Below T_B ZFC and FC curves significantly split. Regarding NSCO and NCCO, due to the limitation of temperature range we were not able to present the behavior of ZFC and FC curves above 380 K. On the other hand, since the splitting temperatures for NSCO and NCCO are higher compared to NCO it seems that Blocking temperatures and Curie temperatures are higher than those of NCO.

Possible formation of vacancies and defects near surface region and grain boundaries in crystal structure are important in stabilizing ferromagnetism due to the discontinuity of magnetic moment configuration in the system. Therefore, while some of imperfections can assist to ferromagnetism some of them may disturb it in this context[50]. Because the size of nanoparticles is small the fraction of the surface atoms is high in nanoparticle systems[51]. Hence, remarkable contribution to magnetization arises from the surface. However, different types of

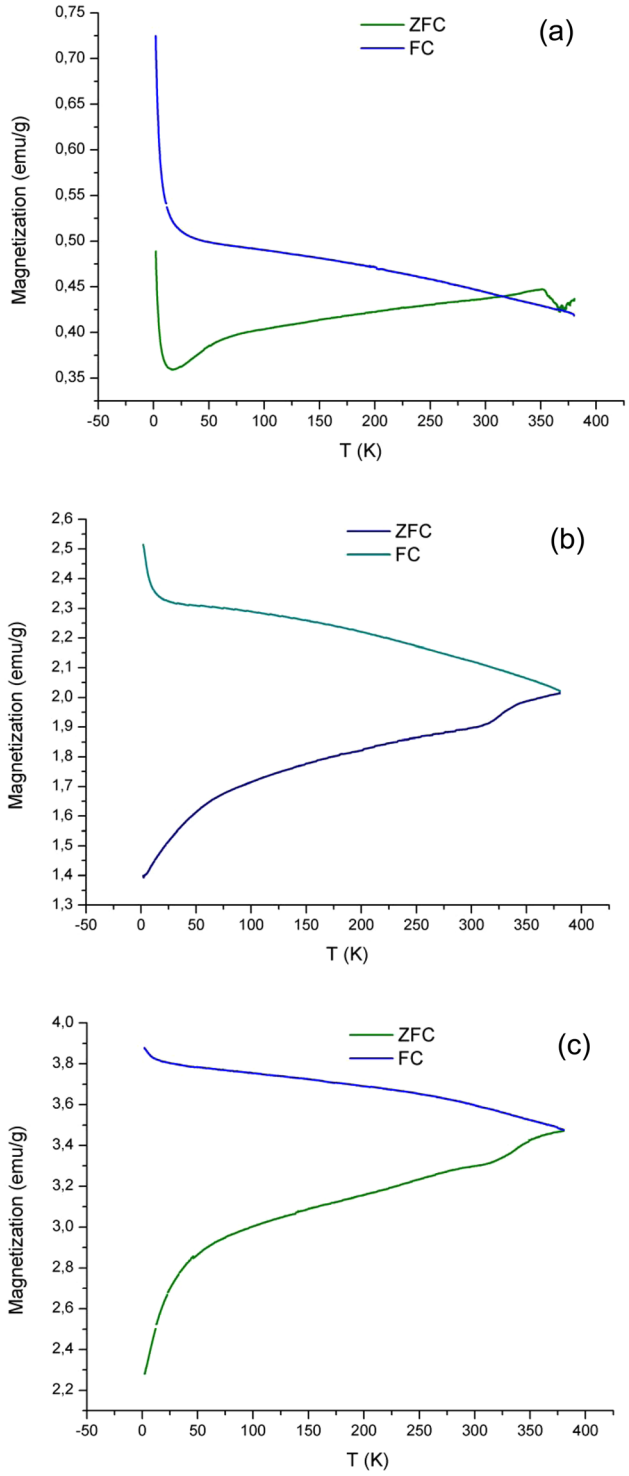

Figure 14. Temperature dependent magnetization (M-T) curves of (**a**) NCO, (**b**) NSCO, and (**c**) NCCO.

defects and imperfections such as lattice disorders, dangling bonds, and vacancies are present at the surface that causes to unbalanced broken spins[52,53]. This is the origin of the surface magnetization which is a generic property of nanoparticles[54].

Mechanical milling causes for structural disorders in grains and their boundaries. Due to gradually increasing temperature some of defects inside the grains are able to move to grain boundaries[55]. Hence, the degrees of disorders near the surface region will enhance and lead to pin mobile charges. Due to the localization of charged particle resistivity will be increased[56] as evidenced by decrease of dielectric loss in this context, which leads to enhance the soft ferromagnetic behaviour in some sense.

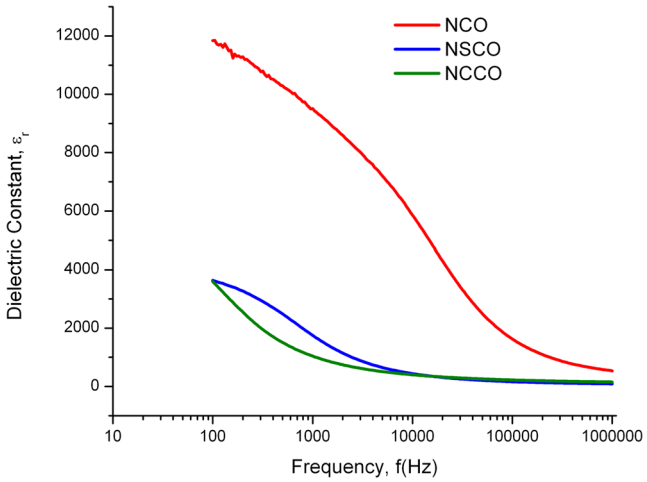

Figure 15. Variation of relative dielectric constant (ε_r) of NCO, NSCO, and NCCO by frequency.

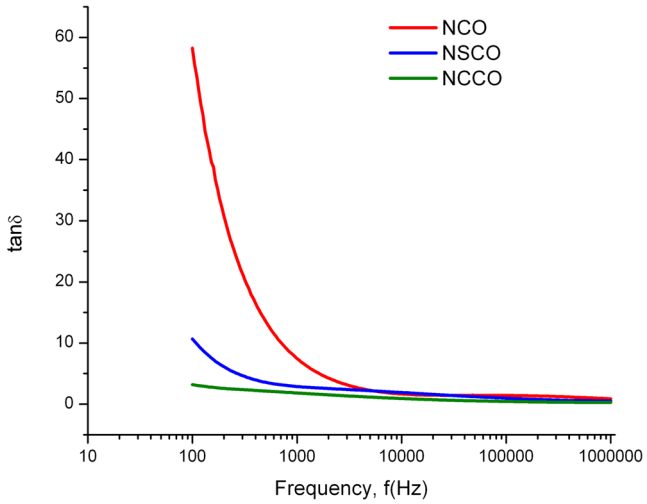

Figure 16. Variation of dielectric loss tangent of NCO, NSCO, and NCCO by frequency.

According to above discussion magnetization vs. magnetic field (M-H) hysteresis curve demonstrates that all the samples are soft ferromagnetic at room temperature. Low coercive fields are attributed to that magnetic domain walls can easily migrate, so the domains are reversed by low applied magnetic field. Additionally, they are well saturated even at low field. Moreover, there is small energy loss during magnetic cycling. Hence, such kinds of materials having slim M-H hysteresis loops are called as soft ferromagnetics. Substitution of Sr or Ca for Nd site seems to improve magnetic properties. Compared to parent $NdCoO_3$ (NCO) both double remanence magnetization ($2M_r$) and double coercivity ($2H_C$) are enhanced. $2M_r$-$2H_C$ values of NCO, NSCO, and NCCO are 4.22–348, 4.45–477, and 4.40 emu/g-361 Gauss, respectively. Therefore, since these soft ferromagnets require low energy to realign the magnetic domains for switching they may have potential applications for recording heads, magnetic cores, and transformers.

Dielectric relaxation of various perovskite type materials arises from conduction or dipolar origins[57]. Room temperature dielectric properties were carried out in the range of 100 Hz–1 MHz. Figure 15 shows relative dielectric constants which decreases with increasing frequency. Low frequency dielectric behavior is attributed to the space charge polarization, interfacial polarization and mobile charges. Since such polarization and mobile charges are not able to follow the electric signal at high frequencies, the dielectric constant decreases and stabilizes beyond 10 kHz for modified samples.

Figure 16 presents the dielectric loss. Loss tangent values decrease by increasing frequency by the same sense of dielectric constant. Relatively high conducting behavior at low frequencies is associated with polarization charges and charge exchange between Co ions. Samples having less loss have low dielectric constant. Therefore, higher resistivity of these soft ferromagnetic perovskite oxides will probably utilize them in high frequency device applications.

Conclusions

In the present study, the $NdCoO_3$ (NCO), $Nd_{0.8}Sr_{0.2}CoO_3$ (NSCO) and $Nd_{0.9}Ca_{0.1}CoO_3$ (NCCO) perovskites were manufactured from nitrate salts ball milled for various periods of times from 4 h to 48 h and they were subjected to heat treatment at 1000 °C for 2 h after 48 h milling. After all processes and analyses for NCO, NSCO and NCCO powders, for the first time, these materials were synthesised at nanocrystalline form by mechanical alloying technique which enable in only two steps, milling and heating. The following more conclusions are drawn:

1. NCO, NSCO and NCCO perovskites were successfully synthesized by mechanical alloying technique without any additional processes like other techniques.
2. The homogeneity of the NCO perovskite progressively continued with increasing milling time up to 48 h. Then, it was observed that each constituent was uniformly dispersed and the initial powders transformed into spherical form from irregular shapes.
3. The sharp crystalline peaks of XRD disappeared with increasing milling time and the perovskite peaks were obtained after heating at 1000 °C for 2 h for 48 h milling.
4. The crystallite sizes of the NCO, NSCO and NCCO perovskites decreased during mechanical milling. Thus, they were determined 18.2 nm, 19.2 nm and 19.7 nm, respectively, after 48 h of milling time. These values were confirmed by TEM.
5. All the materials exhibited soft ferromagnetic properties at room temperature.
6. The dielectric constants of the NCO, NSCO and NCCO perovskites decreased with increasing frequency.

References

1. Mandal, S. K. *et al*. Effect of nanometric grain size on electronic-transport, magneto-transport and magnetic properties of $La_{0.7}Ba_{0.3}MnO_3$ nanoparticles. *J. Phys. Condens. Matter* **20**, 385203 (2008).
2. Orlovskaya, N. *et al*. Ferroelasticity and hysteresis in $LaCoO_3$ based perovskites. *Acta Materialia* **50**, 715–723 (2002).
3. Gonzalez, A. *et al*. Synthesis of high surface area perovskite catalysts by non-conventional routes. *Catalysis Today* **33**, 361–369 (1997).
4. Kostogloudis, G. C. *et al*. Crystal structure, thermal and electrical properties of $Pr_{1-x}Sr_xCoO_{3-\delta}$ (x = 0, 0.15, 0.3, 0.4, 0.5) perovskite oxides. *Solid State Ionics* **106**, 207–218 (1998).
5. Kostogloudis, G. C. *et al*. Electronic conductivity in the $Pr_{1-x}Sr_xCo_{1-y}Mn_yO_{3-\delta}$ system. *Solid State Ionics* **118**, 241–249 (1999).
6. Kundu, A. K. *et al*. Spin-glass behavior in $Pr_{0.7}Ca_{0.3}CoO_3$ and $Nd_{0.7}Ca_{0.3}CoO_3$. *J. Solid State Chem.* **179**, 923–927 (2006).
7. Hosoya, Y. *et al*. Ozone detection in air using $SmFeO_3$ gas sensor. *Sensors and Actuators B* **108**, 198–201 (2005).
8. Carotta, M. C. *et al*. Gas-sensitive electrical properties of perovskite-type $SmFeO_3$ thick films. *Sensors and Actuators B* **48**, 270–276 (1998).
9. Vashook, V. *et al*. Electrical conductivity and oxygen nonstoichiometry in the double B mixed $La_{0.6}Ca_{0.4}Mn_{1-x}Co_xO_{3-\delta}$ perovskite system. *J. Alloys and Compounds* **487**, 577–584 (2009).
10. James, M. *et al*. Oxygen vacancy ordering in strontium doped rare earth cobaltate perovskites $Ln_{1-x}Sr_xCoO_{3-\delta}$ (Ln = La, Pr and Nd; x > 0.60). *Materials Research Bulletin* **40**, 990–1000 (2005).
11. Patil, A. *et al*. Heat capacities of $RCoO_3$(s) (R = La, Nd, Sm Eu, Gd, Tb, Dy and Ho) by differential scanning calorimetry. *Thermochimica Acta* **465**, 25–29 (2007).
12. Zhou, A. J. *et al*. Thermoelectric properties of perovskite-type oxide $La_{1-x}Sr_xCoO_3$ (x = 0, 0.1) prepared by solid state reactions. *Mater. Science and Engineering B* **128**, 174–178 (2006).
13. Brinks, H. W. *et al*. Structure and Magnetism of $Pr_{1-x}Sr_xCoO_{3-\delta}$. *J. Solid State Chem.* **147**, 464–477 (1999).
14. Benali, A. *et al*. Study of critical behavior of perovskite $La_{0.8}Ca_{0.2-x}Pb_xFeO_3$ (x = 0.0, 0.1 and 0.2) compounds. *J. Alloys and Compounds* **638**, 305–312 (2015).
15. Zhang, L. *et al*. Colossal electroresistance and magnetoresistance effect in polycrystalline perovskite cobaltites $Nd_{1-x}Sr_xCoO_3$ (x = 0.1, 0.2, 0.3). *Materials Research Bulletin* **48**, 1088–1092 (2013).
16. Moon, J.-W. *et al*. Ca-doped $HoCoO_3$ as p-type oxide thermoelectric material. *Materials Letters* **48**, 225–229 (2001).
17. Pelloquin, D. *et al*. Partial substitution of rhodium for cobalt in the misfit $[Pb_{0.7}Co_{0.4}Sr_{1.9}O_3]^{RS}[CoO_2]_{1.8}$ oxide. *J. Solid State Chem.* **178**, 769–775 (2005).
18. Hashimoto, H. *et al*. Temperature dependence of electrical and thermal properties for perovskite-type rare earth cobalt oxide solid solutions $Pr_{1-x}Tb_xCoO_3$ and their metal–insulator transition behavior. *J. Alloys and Compounds* **494**, L3–L6 (2010).
19. Mineshige, A. *et al*. Crystal Structure and Metal–Insulator Transition of $La_{1-x}Sr_xCoO_3$. *J. Solid State Chem.* **121**, 423–429 (1996).
20. Nakatsugawa, H. *et al*. Evidence for the two-dimensional hybridization in $Na_{0.79}CoO_2$ and $Na_{0.84}CoO_2$. *J. Solid State Chem.* **177**, 1137–1145 (2004).
21. Fujine, Y. *et al*. Anomalous phonon scattering by Jahn–Teller active Co intermediate spins in $LaCoO_3$ and doped $LaCoO_3$. *Physica B* **359–361**, 1360–1362 (2005).
22. Troyanchuk, I. O. *et al*. Phase Transformations in $Pr_{1-x}Sr_xCoO_3$. *J. Experimental and Theoretical Phys. Letters* **84**(3), 151–155 (2006).
23. Muthuselvam, I. P. *et al*. Grain size dependent magnetization, electrical resistivity and magnetoresistance in mechanically milled $La_{0.67}Sr_{0.33}MnO_3$. *J. Alloys and Compounds* **511**, 22–30 (2012).
24. Fondado, A. *et al*. Synthesis, characterization, magnetism and transport properties of $Nd_{1-x}Sr_xCoO_3$ perovskites. *J. Alloys and Compounds* **323–324**, 444–447 (2001).
25. Bhaskar, A. *et al*. Electrical properties of fluorine-intercalated layered perovskite oxide: $La_{1.4}Sr_{1.6}Mn_2O_7F_2$. *J. Alloys and Compounds* **623**, 324–327 (2015).
26. Thakur, R. *et al*. Specific heat of rare earth cobaltates $RCoO_3$ (R = La, Pr and Nd). *J. Alloys and Compounds* **516**, 58–64 (2012).
27. Robert, R. *et al*. Crystal structure, morphology and physical properties of $LaCo_{1-x}Ti_xO_{3\pm\delta}$ perovskites prepared by a citric acid assisted soft chemistry synthesis. *Acta Materialia* **58**, 680–691 (2010).
28. Zhang, L. *et al*. Critical behavior of the half-doped perovskite $Pr_{0.5}Sr_{0.5}CoO_{3-\Delta}$. *J. Alloys and Compounds* **588**, 294–299 (2014).
29. Ganguly, R. *et al*. Influence of the size of dopant ion on ferromagnetic behavior of $Ln_{0.7}A_{0.3}CoO_3$ system [Ln = La, Nd; and A = Ca, (Ca, Sr), Sr, (Sr, Ba), Ba]. *Physica B* **271**, 116–124 (1999).
30. Kostogloudis, G. C. *et al*. Preparation and Characterization of $Pr_{1-x}Sr_xMnO_{3\pm\delta}$ (x = 0, 0.15, 0.3, 0.4, 0.5) as a Potential SOFC Cathode Material Operating at Intermediate Temperatures (500–700 °C). *J. European Ceramic Society* **17**, 1513–1521 (1997).
31. Cheah, M. *et al*. The Jahn–Teller distortion and cation ordering in the perovskite Sr_2MnSbO_6. *J. Solid State Chem.* **179**, 1775–1781 (2006).
32. Bukhari, S. M. *et al*. Tuneability of $Sm_{(1-x)}Ce_xFeO_{3\pm\lambda}$ perovskites: Thermal stability and electrical conductivity. *Solid State Ionics* **180**, 198–204 (2009).

33. Chau, N. *et al*. Tho, Structure, magnetic, magnetocaloric and magnetoresistance properties of $La_{1-x}Pb_xMnO_3$ perovskite. *Physica B* **327**, 214–217 (2003).
34. Cheng, J. A. *et al*. Energetics of $La_{1-x}A_xCrO_{3-\delta}$ perovskites (A = Ca or Sr). *J. Solid State Chem.* **178**, 234–244 (2005).
35. Ghasdi, M. *et al*. CO sensitive nanocrystalline $LaCoO_3$ perovskite sensor prepared by high energy ball milling. *Sensors and Actuators B* **148**, 478–485 (2010).
36. Sorescu, M. *et al*. Investigation of $LaFeO_3$ perovskite growth mechanism through mechanical ball milling of lanthanum and iron oxides. *J. Mater. Sci.* **46**, 6709–6717 (2011).
37. Kun, R. *et al*. Structural and thermoelectric characterization of Ba substituted $LaCoO_3$ perovskite-type materials obtained by polymerized gel combustion method. *J. Alloys and Compounds* **579**, 147–155 (2013).
38. Kaliaguine, S. *et al*. Perovskite-type oxides synthesized by reactive grinding: Part I. Preparation and characterization. *Applied Catalysis A: General* **209**, 345–358 (2001).
39. Manh, D. H. *et al*. $La_{0.7}Ca_{0.3}MnO_3$ perovskite synthesized by reactive milling method: The effect of particle size on the magnetic and electrical properties. *J. Alloys and Compounds* **491**, 8–12 (2010).
40. Melo, D. S. *et al*. Lanthanum-based perovskites obtained by the polimeric precursor method. *J. Mater. Sci.* **43**, 551–556 (2008).
41. Daivajna, M. D. *et al*. Electrical, magnetic and thermal properties of $Pr_{0.6-x}Bi_xSr_{0.4}MnO_3$ manganites. *J. Alloys and Compounds* **588**, 406–412 (2014).
42. Cao, Y. *et al*. Structure, morphology and electrochemical properties of $La_xSr_{1-x}Co_{0.1}Mn_{0.9}O_{3-\delta}$ perovskite nanofibers prepared by electrospinning method. *J. Alloys and Compounds* **624**, 31–39 (2015).
43. Liu, X. *et al*. Acetone gas sensing properties of $SmFe_{1-x}Mg_xO_3$ perovskite oxides. *Sensors and Actuators B* **134**, 483–487 (2008).
44. Chen, W. *et al*. Salt-assisted combustion synthesis of highly dispersed perovskite $NdCoO_3$ nanoparticles. *Mater. Letters* **61**, 397–400 (2007).
45. Gogebakan, M. *et al*. Formation of new Cu-based nanocrystalline powders by mechanical alloying technique. *Powder Technology* **247**, 172–177 (2013).
46. Malavasi, L. *et al*. $NdCoO_3$ perovskite as possible candidate for CO-sensors: thin films synthesis and sensing properties. *Sensors and Actuators B* **105**, 407–411 (2005).
47. Zhou, W. *et al*. Progress in understanding and development of $Ba_{0.5}Sr_{0.5}Co_{0.8}Fe_{0.2}O_{3-\delta}$-based cathodes for intermediate-temperature solid-oxide fuel cells: a review. *J. Power Sources* **192**, 231–246 (2009).
48. Kursun, C. *et al*. Characterization of nanostructured Mg–Cu–Ni powders prepared by mechanical alloying. *J. Alloys and Compounds* **619**, 138–144 (2015).
49. Taguchi, H. *et al*. Spin State of Cobalt Ion in $Nd(Cr_{1-x}Co_x)O_3$. *J. Solid State Chem.* **122**, 297 (1996).
50. Chattopadhyay, S. *et al*. Defects induced ferromagnetism in Mn doped ZnO. *J. Magn. Magn. Mater.* **323**, 363–368 (2011).
51. Batlle, X. *et al*. Finite-size effects in fine particles: Magnetic and transport properties. *J. Phys. D* **35**, R15–R42 (2002).
52. Ho, C.-H. *et al*. Size-dependent magnetic properties of PtMn nanoparticles. *IEEE Trans. Magn.* **42**, 3069–3071 (2006).
53. Dobrynin, A. N. *et al*. Critical size for exchange bias in ferromagnetic-antiferromagnetic particles. *Appl. Phys. Lett.* **87**, 012501 (2005).
54. Issa, B. *et al*. Magnetic Nanoparticles: Surface Effects and Properties Related to Biomedicine Applications. *Int. J. Mol. Sci.* **14**, 21266–21305 (2013).
55. Dutta, S. *et al*. Annealing effect on nano-ZnO powder studied from positron lifetime and optical absorption spectroscopy. *J. Appl. Phys* **100**, 114328 (2006).
56. Lin, H. J. *et al*. A study of the grain size and electric properties of Mn-doped ZnO thin films grown by plasma-assisted molecular beam epitaxy. *Phys. Stat. Sol.* **6**, 1468–1471 (2009).
57. Katari, V. *et al*. Effect of Preparation Conditions on Magnetic and Dielectric Properties of Y_2MMnO_6 (M = Co, Ni). *J. Am. Ceram. Soc.* **99**, 499–506 (2016).

Acknowledgements

We would like to thank Kahramanmaras Sutcu Imam University for financial support of the research programme (Project No. 2014/4-10 YLS). SPECLAB at the University of Puerto Rico is also acknowledged for using dielectric and magnetic measurement facilities.

Author Contributions

C.K. conceived and designed the study. C.K. and E.U. wrote the main manuscript text. M.G. helped the comments. M.S.B. analysed the magnetic and electrical properties. F.S.U. drew Figures 1–4.

Additional Information

Competing Interests: The authors declare no competing interests.

Publisher's note: Springer Nature remains neutral with regard to jurisdictional claims in published maps and institutional affiliations.